Control of MEMS vibration modes with Pulsed Digital Oscillators: Part II — Simulation and experimental results

Jordi Ricart[1], Joan Pons-Nin[1], Elena Blokhina[2], Sergi Gorreta[1], Jorge Hernando[3], Tomas Manzaneque[3], Jose Luis Sanchez-Rojas[3], Orla Feely[2], Manuel Dominguez[1*]

[1] Micro and Nano Technologies Group, Universitat Politécnica de Catalunya, Spain
[2] School of Electrical, Electronic and Mechanical Engineering, University College Dublin, Ireland
[3] Electronic Engineering Dept., Universidad de Castilla la Mancha, Spain

[*] corresponding author email: mpumar@eel.upc.es

***Abstract*— This paper extends our previous work on the selective excitation of mechanical vibration modes in MEMS devices using Pulsed Digital Oscillators. It begins by presenting extensive simulation results using the set of iterative maps that model the system and showing that it is possible to activate two or three spatial modes (resonances) of the mechanical structure with a Pulsed Digital Oscillator (PDO). The second part of this paper presents experimental results corroborating the theory and simulation results. It is shown that it is possible to separately excite vibration modes of the device by setting a few parameters of the PDO structure such as the sampling frequency and the sign of the feedback loop.**

***Index Terms*— Microelectromechanical systems (MEMS), microresonators, sigma-delta modulation, multimode control.**

I. Introduction

The detection of frequency shifts or amplitude changes in vibrating MEMS devices in response to an external stimulus is a mechanism widely used in applications such as the sensing of pressure, mass change, acceleration, etc. Many efforts have been made in recent years to improve the perfomance of MEMS resonant sensors (i.e. see [1], [2] and papers cited there). For instance, the sensitivity of such sensors often depends on the resonant frequency of the MEMS structure, which is usually excited in one of its mechanical modes.

In the particular case of gravimetric resonant sensors, several works show that operating at higher frequencies (or in higher order modes) can be an effective way to increase their sensitivity to mass changes [3]–[5]. Parametric resonance amplification is an example of an efficient technique that allows the excitation of the same mechanical structure at a higher frequency to improve sensitivity [6], [7]. Moreover, the activation of higher vibration modes to increase performance has been also reported in atomic force microscopes [8], [9] and in piezoelectric sensors and actuators [10], where electrodes have been specifically designed to activate certain modes. Additionally, in gyroscope applications it is often desired to avoid the activation of certain resonant modes of the inertial mass [11], [12].

One can conclude that the selective activation of different vibration modes of a MEMS resonator is a suitable way to improve performance in a large number of applications. Thus, the objective of this paper is to show that Pulsed Digital Oscillators may be an easy and efficient tool for this purpose.

Pulsed Digital Oscillators (see fig. 1) are structures that can work as mass-change resonant sensors [13], [14]. Part I of this work [15] describes the theory that demonstrates how PDOs may be used to selectively excite self-sustained resonant mechanical modes in MEMS structures. To this effect, it has been shown there that a beam cantilever can be described through a set of iterative equations, with each iterative map responsible for a spatial vibration mode. It has also been proved that for a spatial mode there will be regions of oscillations (with large amplitude limit cycles) and 'forbidden' or anti-oscillation regions (with small amplitude limit cycles). The presence of these opposite regions opens the possibility of the selective excitation of one of the spatial modes if a few controlling parameters of the PDO system are chosen correctly.

The main purpose of the current paper is to present results of numerical simulations and experiments in order to prove that several spatial modes (or resonances) of a MEMS structure can be controlled easily by the feedback loop parameters of the PDO structure. At first, numerical simulations are mostly focused on the simplest, but common, case when the first two mechanical modes are taken into consideration (Sec II). However, we consider as well in general outline the particular case of the third resonance mode (Sec. III). The results of numerical simulations are presented and discussed. We show the planes spanned by controlling parameters of the system with distributions of the oscillation amplitudes and frequencies and discuss at which values of the sampling frequency the excitation of higher spatial modes is possible.

Later, the experimental work validating the proposed ap-

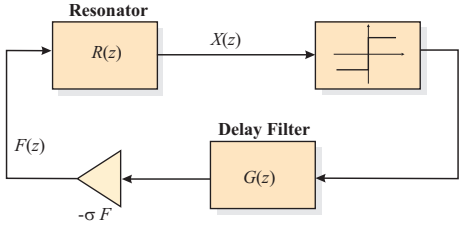

Fig. 1. General single feedback topology of the pulsed digital oscillator. The circuit topology consists of a resonator, a 1-bit quantizer (sign function), and a delay filter, $G(z) = z^{-(L+1)}$. The position of the MEMS resonator is evaluated at each sampling time, and short pulses of force are applied to it.

proach is presented. We prove the feasibility of exciting different vibration modes in a MEMS cantilever by working with the controlling parameters of a PDO. In order to approximately locate the different mechanical vibration modes of the MEMS resonator used, FEM, discrete-time simulations and vibrometer-only measurements of the structure have been first carried out (Sec. IV). Then, according to the theory previously derived, several settings for sampling frequency, sign and delays in the PDO feedback loop are applied to our PDO experimental framework (Sec. V). The activation of each resonant mode is tested with a scanning laser Doppler vibrometer. This measurement technique allows us to obtain accurate information about the displacement and velocity with time (or frequency) and position along the top surface of the device under test. The corresponding results are in good agreement with the theory and simulations.

II. Results of numerical simulations

A. Statement of the problem

Let us first give here a brief overview of the problem. In order to obtain a lumped model of different resonant modes of the mechanical structure in the PDO, Part I of this paper [15] analyses a partial differential equation (PDE) of a cantilever. An order-reduction strategy has been applied to the PDE consisting of discretising the initial distributed system by means of a set of spatial eigenmode functions $\psi_i(\xi)$. As a result, a set of ordinary differential equations has been obtained that represents the dynamics of each spatial mode as the mass-spring-damper equation with appropriate parameters.

This system is subjected to pulsed excitation. Between two sampling instants the resonator moves freely, and at each sampling event its velocity is instantaneously changed by the applied delta-pulse. This allows a description of an individual spatial mode in terms of an iterative map with the dimensionless displacement and velocity as dynamical variables:

$$\begin{pmatrix} x_{i,n+1} \\ v_{i,n+1} \end{pmatrix} = \alpha_i \mathbf{R}(2\pi f_i) \begin{pmatrix} x_{i,n} \\ v_{i,n} \end{pmatrix} + \begin{pmatrix} 0 \\ \zeta_i \end{pmatrix} b_{n-L}\,, \quad (1)$$

for $i = 1, \ldots, M$ being the number of a spatial mode. In these equations, $\mathbf{R}(\theta) = \left(\begin{smallmatrix} \cos\theta & -\sin\theta \\ \sin\theta & \cos\theta \end{smallmatrix}\right)$ is the rotation matrix by the angle θ, $L+1$ is the number of delay blocks in the feedback loop and b_n is the sequence of signs of the resonator position $b_n = \operatorname{sgn} \sum_{i=1}^{M} x_i(\tau_n)\psi_i(\xi_s)$ expressed through the basis functions ψ_i of spatial modes. The parameters in (1) are expressed through the sampling frequency f_s and the parameters of the mass-spring-damper equations for spatial modes: γ (dissipation), Ω_i^2 (the frequency of the ith mode) and F_{0i} (the amplitude of the external driving).

$$\begin{aligned} \rho_i &= \frac{\gamma}{2\Omega_i^2}\,, & f_i &= \frac{\Omega_i^2}{f_s}\sqrt{1-\rho_i^2}\,, \\ \zeta_i &= \frac{\sigma F_{0i}}{\Omega_i^2\sqrt{1-\rho_i^2}}\,, & \alpha_i &= \exp\left(\frac{-2\pi\rho_i f_i}{\sqrt{1-\rho_i^2}}\right)\,, \end{aligned} \quad (2)$$

where ρ_i is the dimensionless damping parameter, f_i is the normalised sampling ratio in terms of the paper [16] (or normalised frequency in terms of the paper [17]), ζ_i is the normalised increment (note that it depends on the sign of the feedback loop σ) and α_i is the contraction factor. In (1), the first letter of the index, i.e. "i", refers to the number of a spatial mode, and the second letter, i.e. "n", refers to the iteration number.

Let us emphasise the particular case when the first two spatial modes are considered. It is very convenient to establish the correlation between the parameters that refer to the first and the second modes in explicit form. So let us introduce the ratio of the spatial frequencies of the modes as follows:

$$\nu = \frac{\Omega_2}{\Omega_1}\,, \quad (3)$$

and apply it to connect the set of parameters for the modes:

$$\begin{aligned} \rho_2 &= \frac{\rho_1}{\nu^2}\,, \\ f_2 &= \nu^2 f_1 \frac{\sqrt{1-\rho_1^2/\nu^4}}{\sqrt{1-\rho_1^2}} \approx \nu^2 f_1\,, \\ \zeta_2 &= \frac{\mu\,\zeta_1}{\nu^2}\frac{\sqrt{1-\rho_1^2}}{\sqrt{1-\rho_1^2/\nu^4}} \approx \frac{\mu\,\zeta_1}{\nu^2}\,, \\ \alpha_2 &= \alpha_1^{\sqrt{1-\rho_1^2}/\sqrt{1-\rho_1^2/\nu^4}} \approx \alpha_1\,. \end{aligned} \quad (4)$$

For the case of two resonances it is convenient to rewrite the expression for the sequence b_n in the form $b_n = x_{1,n} + \beta x_{2,n}$,

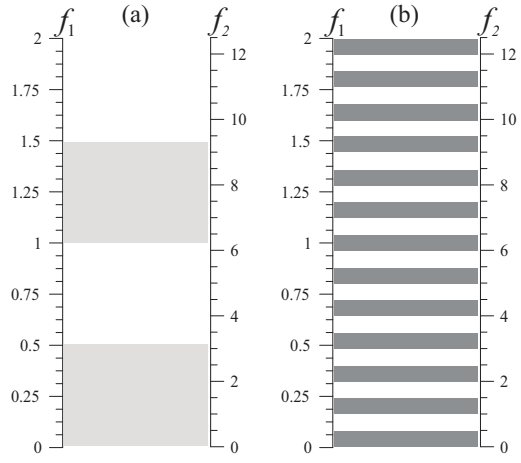

Fig. 2. Regions of the normalised frequencies $f_{1,2}$ that correspond to the oscillation and anti-oscillation regimes of the first (a) and the second (b) spatial modes. The left vertical axis shows the scale of f_1, the right vertical axis shows f_2 for the convenience.

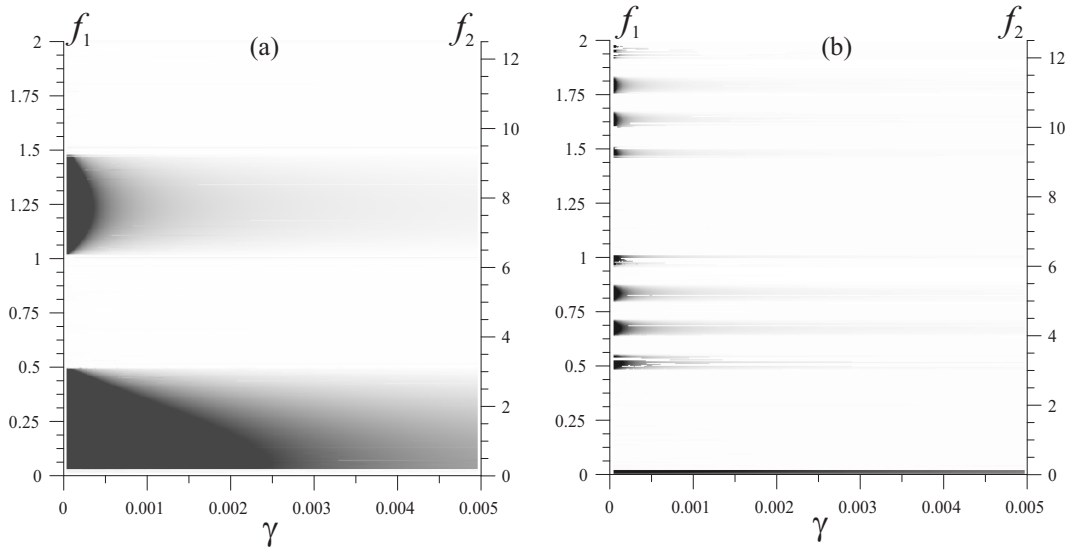

Fig. 3. Plane of parameters (γ, f_1) — the dissipation parameter and the normalised frequency in which the shades of the grey colour show the intensity of oscillations. Plot (a) shows the amplitude of oscillations of the first spatial mode, while plot (b) shows the amplitude of oscillations of the second spatial mode. The actuating and sensing structures are placed at $\xi_s = \xi_a = 1$, $\beta = \mu = -1$.

where $\beta = \psi_2(\xi_s)/\psi_1(x_s)$ is the ratio of the basis functions at the point of position sensing. The coefficient μ is defined as the ratio of the spatial function values at the point of actuation $\mu = \psi_2(\xi_a)/\psi_1(\xi_a)$. Note that from the beginning we have introduced into our theory such parameters as the frequencies of the eigenmodes. As a consequence, the parameters that we use for formulation of the iterative system cannot be considered as independent ones, i.e. we have to change the values of controlling parameters according the expressions (4). For instance, in the experimental set the sampling frequency is measured with respect to the frequency of the fundamental mode (i.e. the first spatial mode with the lowest frequency), thus, the sampling ratio f_1 is given as a "basic" parameter. The value of f_2 can be obtained simply by re-calculating f_1 with the ratio ν.

B. Oscillation and anti-oscillation regimes

As noted in [14], energy can be put into or extracted from the resonator. When the velocity of the resonator is positive, applying a positive impulse leads to an increase in kinetic energy. On the other hand, when the velocity is negative, applying a positive impulse will decrease the energy. Sustained oscillations in the PDO are reached if the feedback sign σ is selected correctly.

This physical mechanism leads to the presence of the oscillation and antioscillation regimes [18] in the iterative equations (1) for a single spatial mode. We will use one of the following terms: *oscillation* mode (or regime) or *oscillations* to refer to large amplitude oscillations when kinetic energy is added to the resonator by the force pulses. We will use the term *anti-oscillation* mode (regime) or *anti-oscillations* to denote very small amplitude oscillations (with corresponding limit cycles situated near the origin) when energy is extracted from the resonator by the force pulses [18].

For an arbitrary number of the delays $L+1$ and the sign σ of the feedback loop, the regions of antioscillations (or regions with no 'tuned' frequency [17]) for a single mode of the PDO are defined by the following expressions:

$$\begin{aligned} \sigma = 1: &\qquad f \in \left(\frac{1+2k}{2(L+1)}, \frac{1+k}{L+1} \right), \\ \sigma = -1: &\qquad f \in \left(\frac{k}{L+1}, \frac{1+2k}{2(L+1)} \right), \end{aligned} \tag{5}$$

for any integer k.

Oscillation and anti-oscillation areas calculated from formula (5) are shown in Fig. 2. The left vertical axis indicates the normalised frequency (sampling ratio) f_1 with respect to the temporal frequency of the first mode and the right vertical axis shows the normalised frequency (sampling ratio) f_2. In Fig. 2(a), the light gray areas correspond to the oscillation regions of the first mode, and in Fig. 2(b) the dark gray region correspond to oscillations of the second mode. The blank areas correspond to the antioscillations for both spatial modes. As is seen from the figure, there will be regions of overlapping, i.e., simultaneous oscillations of the first and second modes, In this case, the output of the PDO can display either the first or the second mode, depending on additional conditions, such as initial conditions or the MEMS geometry parameters.

C. Distribution of the oscillation amplitude for the first and the second mode.

We start with the most standard case when the actuating and sensing systems are placed at the end of the beam. The parameters that describes the structure of the MEMS are the following: $\beta = \mu = -1$. The dynamics of the system (1) are studied in the plane spanned by the controlling parameters (γ, f_1) — the dissipation parameter and the sampling ratio (normalised sampling frequency).

Let us first estimate the contribution of each spatial mode to the overall oscillations. Figure 3 shows the distribution of the oscillation amplitudes in the plane (γ, f_1). The additional

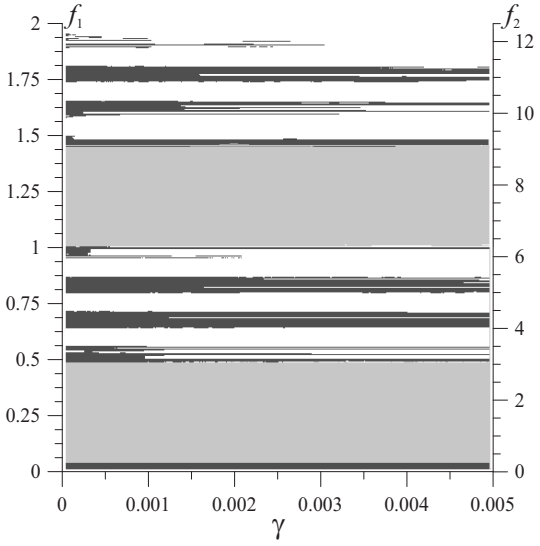

Fig. 4. Plane of parameters (γ, f_1) — the dissipation parameter and the normalised frequency in which the grey shades show the output frequency. The case $f_D \approx f^*_{1,D}$ is shown by the light gray, $f_D \approx f^*_{2,D}$ by the dark grey, and blank regions show that the output frequency f_D corresponds to neither modes frequencies $f^*_{1,2,D}$. The actuating and sensing structures are placed at $\xi_s = \xi_a = 1$, $\beta = \mu = -1$.

vertical axis shows the normalised frequency f_2 for the convenience of readers. Plot 3(a) represents this distribution for the amplitude of the first spatial mode, and plot 3(b) the distribution for the second mode. Figures 3(a) and (b) are calculated with respect to some value of A_{max} in the following way. At each pair of the parameters (γ, f_1), the system (1) is iterated; the obtained amplitudes of oscillations are compared to A_{max} and, based on this comparison, we estimate the magnitude of oscillations and assign a colour to a point (γ, f_1). The higher the amplitude of oscillations, the darker the shade that represents the corresponding point in the plane. All planes presented in the paper are calculated with the zero initial conditions $x_{0,i} = y_{0,i} = 0$.

As seen in Fig. 3, we can divide the plane into parts where the first mode is dominating and parts where the first mode is suppressed. According to the formulas (5), the regions $f_s < 0.5$ and $1 < f_s < 1.5$ correspond to the oscillations of the first mode (however, these regions include a lot of subsets with the oscillations of the second mode as well).

A considerable rise of the second mode amplitude is observed at $0.5 < f_1 < 1$ and $1.5 < f_1 < 2$, i.e. in the regions of the anti-oscillations of the first mode. In general, the maximum amplitude of the second mode is lower than the maximum amplitude of the first one. Note that the device is designed to operate at a high-Q factor, i.e. at small values of the dissipation parameter γ. In the presented planes, bands that represents the intensity of oscillations (of both modes) still exist at higher values of γ, however, the oscillations decay noticeably as the dissipation increases. Note that the stripes in Fig. 3(b) that show the second mode oscillations appear strictly at values of the sampling frequency that correspond to the oscillation regime of the second mode.

D. Frequency of the PDO output

Since the PDO is a digital oscillator, the oscillation frequency can be directly calculated from the output bitstream [14], [17], [18]. The resulting oscillation frequency is $f_{osc} = f_s f_D$, where f_D is the digital frequency extracted from the bitstream.

It was shown in [14] that using the standard linear analysis of the oscillator loop and taking into account the sampled impulse response of the MEMS device, one can get a good approximation of the digital frequency from the expression

$$f^*_{i,D} = \frac{1}{2\pi} \cos^{-1}\left(a_i \cos(2\pi f_i)\right) \in (0,\, 0.5)\ , \qquad (6)$$

where α_i is the contraction factor and f_i is the normalised sampling ratio introduced by the formulas (2) and the index *i* refers to the *i*th eigenmode.

In the previous section we have shown that depending on the sampling ratio and the sign of the feedback term the PDO oscillations can be associated with either the first or the second mode. This conclusion was drawn based on the analysis of the oscillation amplitude after iterating the system (1). In fact, the only output we typically obtain from the PDO is the bitstream provided by the comparator which is the sign of the sampled position of the resonator. This allows us to get the information about the frequency of oscillations, not the amplitude. The important question is: which spatial mode frequency does the output frequency correspond to?

We will use the route suggested in [17] to generate the auxiliary sequence and obtain the digital frequency of oscillations f_D. The q_n sequence is defined as follows

$$q_n = \begin{cases} 1, & \text{if } b_n \neq b_{n+1}\,, \\ 0, & \text{if } b_n = b_{n+1}\,. \end{cases} \qquad (7)$$

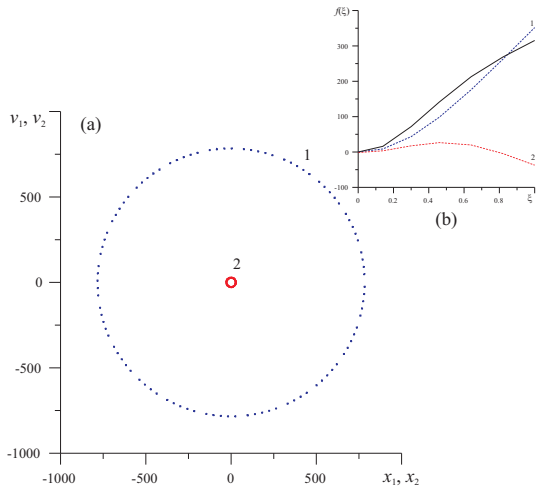

Fig. 5. (a) Typical limit cycles. (1) is the limit cycle displayed by the dynamical variables $(x_{1,n}, v_{1,n})$ that correspond to the first spatial mode, (2) is the limit cycle displayed by the second mode. (b) A typical profile of the beam as a function of the longitudinal coordinate ξ; The dashed line with mark "1" shows the profile that corresponds to the first spatial mode; the dashed line with mark "2" shows the profile that corresponds to the second spatial mode. The actual profile of the beam as the superposition of the two modes is illustrated by the black solid line. $\gamma = 0.005$ and $f_1 = 0.19$.

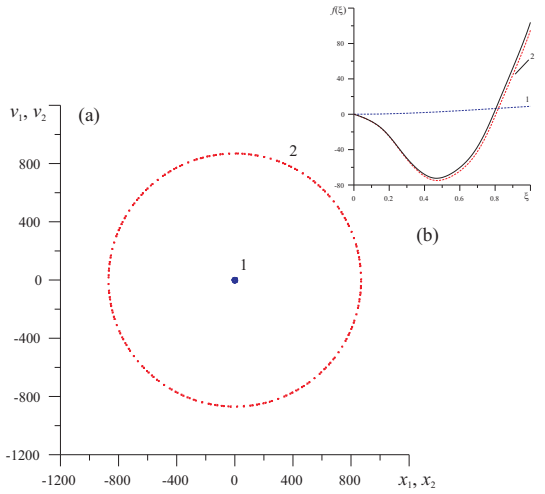

Fig. 6. (a) Typical limit cycles. (1) is the limit cycle displayed by the dynamical variables $(x_{1,n}, v_{1,n})$ that correspond to the first spatial mode, (2) is the limit cycle displayed by the second mode. (b) A typical profile of the beam as a function of the longitudinal coordinate ξ; The dashed line with mark "1" shows the profile that correspond to the first spatial mode; the dashed line with mark "2" shows the profile that correspond to the second spatial mode. The actual profile of the beam as the superposition of the two modes is illustrated by the black solid line. $\gamma = 0.005$ and $f_1 = 0.024$.

The digital frequency of oscillations can now be written as

$$f_D = \frac{1}{2} \cdot \frac{\sum_{n=1}^{N} q_n}{N} \tag{8}$$

Now, at each pair of the parameters (γ, f_1) we can calculate the digital frequency of oscillations by using (8) and compare the result with the theoretical approximation (6). The plane of parameters that shows the output frequency is presented in Fig. (4). The digital frequency of the output is illustrated in the plane in the following manner: the light gray areas show that the output frequency corresponds to the first mode ($f_D \approx f^*_{1,D}$), the dark gray areas to the second mode ($f_D \approx f^*_{2,D}$) and the blank areas indicate that the output is close to neither of them. As expected, there is broad correspondence between the planes shown in fig. 3 and fig. 4: at the values of γ and f_1 when the first spatial mode is excited, the digital frequency of the PDO output is the frequency of the first eigenmode. In addition, when the second spatial mode is excited, the output frequency is the frequency of the second eigenmode. Note that the digital frequency does not correspond to either of the eigenmodes if the parameters are taken from the antioscillation regions for both modes. This implies that the digital frequency extracted from the output allows us to "recognise" what type of oscillations is displayed by the cantilever and associate it with a proper spatial mode.

E. Examples of system dynamics

Now let us illustrate the system dynamics in terms of the first and second spatial mode. Figure 5(a) shows typical limit cycles displayed by the variables $x_{1,n}, v_{1,n}$ (the limit cycle denoted as "1") and $x_{2,n}, v_{2,n}$ (the limit cycle denoted as "2"). The profile of the beam is given in Fig. 5(b). The amplitude of the second mode is smaller than the amplitude of the first one, however it affects the overall profile of the cantilever and causes its distortion.

An opposite example that illustrates the dominance of the second mode is shown in Fig. 6. Note that normally the amplitude of the suppressed mode is significantly smaller than the amplitude of the dominating one, as demonstrated in Fig. 6(a). The actual profile of the cantilever corresponds to the second mode and the distortion of the profile caused by the first one is negligible (see Fig. 6(b)).

F. Control of two resonant modes

In the previous sections we have studied the standard case when both the actuating and sensing structures are placed at

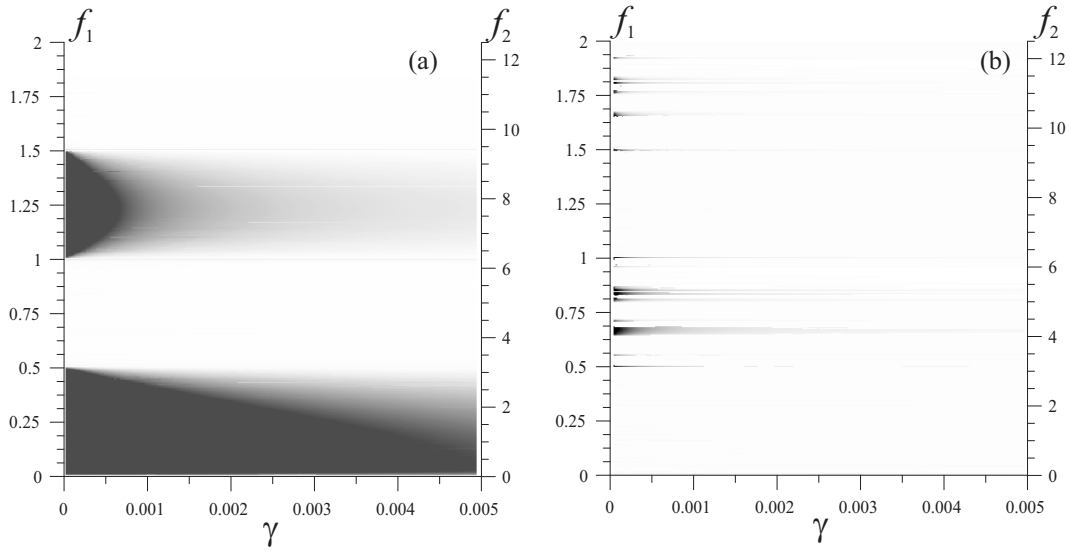

Fig. 7. Plane of parameters (γ, f_1) — the dissipation parameter and the normalised frequency in which the shades of the grey colour show the intensity of oscillations. Plot (a) shows the amplitude of oscillations of the first spatial mode, while plot (b) shows the amplitude of oscillations of the second spatial mode. The actuating and sensing structures are at $\xi_s = \xi_a \approx 0.88$, $\beta = \mu = -0.5$.

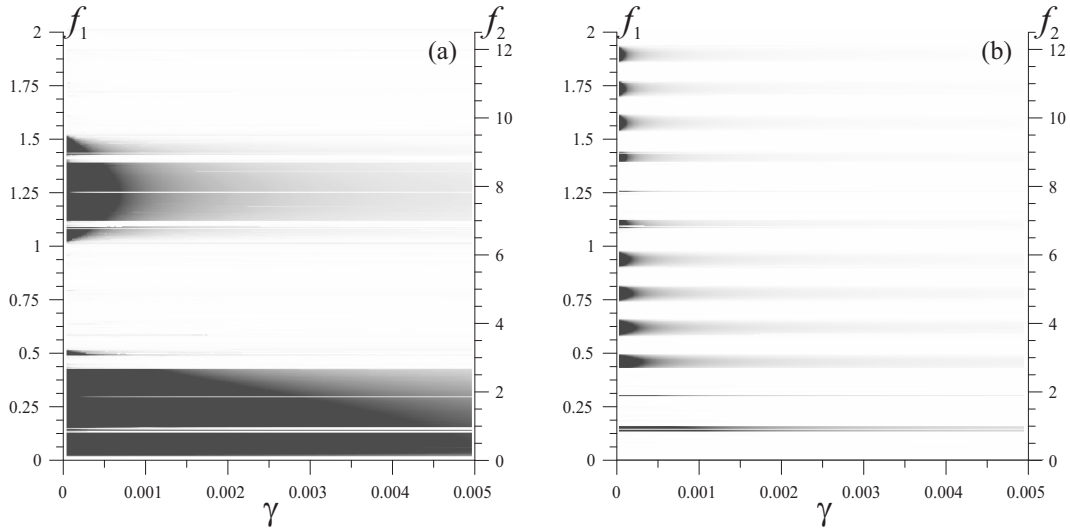

Fig. 8. Plane of parameters (γ, f_1) — the dissipation parameter and the normalised frequency in which the shades of the grey colour show the intensity of oscillations. Plot (a) shows the amplitude of oscillations of the first spatial mode, while plot (b) shows the amplitude of oscillations of the second spatial mode. The actuating and sensing structures are at $\xi_s = 0.3, \xi_a = 1$, $\beta = 3.85, \mu = -1$.

the end of the cantilever. Next, we consider what rearrangements in the entire picture of the spatial modes may be caused by minor shifting of the sensing and actuating systems.

The choice of the parameters β and μ considerably influences the systems behaviour. The first parameter defines the proportion of the modes in the sequence of the sampled resonator position. The value of β should guarantee that the contribution of both modes to the measured position are of the same order. The second parameter, μ, is responsible for the "portion" of the external driving that is received by each mode.

Figure 7 shows the plane of parameters with the amplitude distributions of the first and the second spatial modes (cases (a) and (b)). The plots are calculated at $\xi_s = \xi_a \approx 0.88$, which means that the actuating (and sensing) points are shifted a little from the edge of the beam. The coefficients in this case are $\beta = \mu = 0.5$. This change of β and μ does not affect the first mode, however, by comparing of Fig. 7(b) with Fig. 3(b) one can conclude that the intensity of oscillations that correspond to the second spatial mode reduced.

This can be explained qualitatively as follows: the amplitude of oscillations depends on the amplitude of the external driving (or on the normalised increment Y_i in terms of the map (1)). The increment Y_i is defined in turn by the function $\psi_i(x_a)$. In the region $0.8 < \xi < 1.0$, the function $\psi_2(\xi)$ varies over a wide range of values from 0 to -2, whereas the function $\psi_1(\xi)$ changes a little. The closer the actuation point to $\xi_a \approx 0.78$ (the zero of the function ψ_2), the smaller the value of the increment Y_2 that is responsible for the second mode and the smaller the "portion" of the external driving that is received by the this mode.

Next, it is natural to consider the special case when the sensing and actuating systems are separated and placed at different points of the microcantilever. By adjusting the points ξ_s (or the parameter β) and ξ_a (or the parameter μ), one can achieve better control of the excitation or suppression of higher modes. For instance, one can put the sensing system at $\xi_s = 0.3$, where the function $\psi_2(\xi_s)$ has a large value than $\psi_1(\xi_s)$. Thus, we can expect that oscillations corresponding to the second resonant mode will be significant.

The example illustrated by Fig. 8 was calculated for $\xi_s = 0.3$ and $\xi_a = 1$ ($\beta = 3.85$ and $\mu = -1$). In this case, there are many regions with oscillations that correspond to the second resonant mode (see fig. 8(b)). Moreover, these regions appear at the values of the sampling ratio $0 < f_1 < 0.5$ and $1.0 < f_1 < 1.5$, i.e. in the region where we normally observed only the first mode (compare with Fig. 3).

III. Control of three resonant modes

The aim of this section is to extend the theory and results presented earlier to the case of three resonances. It is known that sensors that utilise higher resonant modes can carry out more precise measurements, since the higher the resonant frequency of the device, the more sensitive it is to a change in

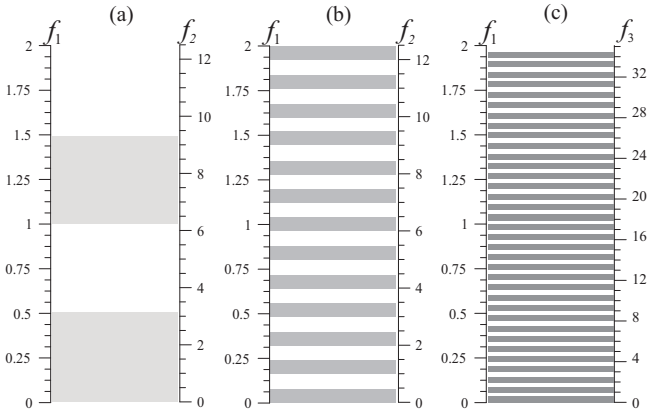

Fig. 9. Normalised frequencies $f_{1,2,3}$ that correspond to the regions of oscillation (in gray) and anti-oscillation (in white) modes for the first (a), second (b) and third (c) spatial modes of the cantilever.

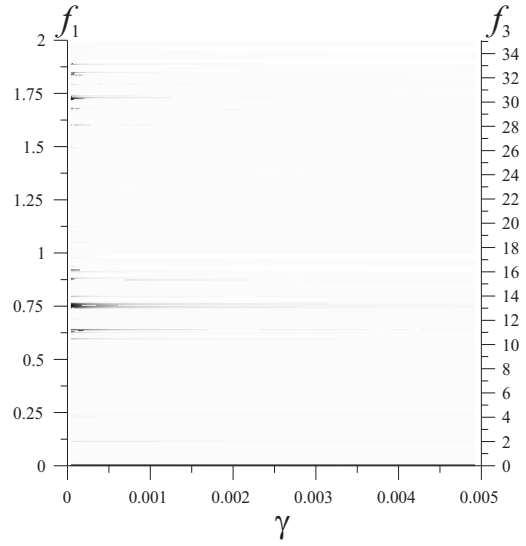

Fig. 10. Plane of parameters (γ, f_1) in which the shades of the grey colour show the amplitude of oscillations of the third spatial mode. The actuating and sensing structures are at $\xi_s = 1, \xi_a = 1$, $\beta = -1$, $\beta' = 1$, $\mu = -1$ and $\mu' = 1$.

the external stimulus. It follows that one way to improve the resolution of measurements is to switch to a higher mechanical mode of the same sensor.

In order to examine three resonances, we include the third pair of iterative equations from (1) with appropriate parameters and incorporate the additional coefficients β' and μ' that describe the relative contribution of the third mode to the position sensing and cantilever actuation. The sequence of the sampled position of the resonator now is

$$s_n = \text{sign}\{y_1(nT) + \beta y_2(nT) + \beta' y_3(nT)\}\,, \qquad (9)$$

The parameters of the third system are defined by (2) in the same manner as in the previous case with two modes.

We may suggest two assumptions concerning the frequency of the third resonance. The first one is to assume that the third mode frequency f_{03} ($f_{03} > f_{02}$) follows from the 1D theory that was presented in our previous work. The coefficients that describe the actuation and sensing systems are $\mu' = \psi_3(\xi_a)/\psi_1(\xi_a)$ and $\beta' = \psi_3(\xi_s)/\psi_1(\xi_s)$.

However we should note that a real MEMS cantilever is a more complicated structure than a simple 1D beam and it is capable of demonstrating torsional deflections as well. More general analysis of the structure shows that there are a number of mechanical modes that include 3D motion of the plate with frequencies that could be less than the frequency f_{03} given by the 1D theory. Thus, the other possibility is to introduce the frequency of the mode f_{03} and the coefficients μ' and β' based upon results obtained from experiments, 3D modelling or any additional assumptions. We have chosen here the third resonance predicted by the 1D theory developed earlier.

The results presented earlier have shown that the primary parameter that is responsible for "switching" from the fundamental first mode to the second mode is the sampling ratio (normalised frequency). Figure 2 has shown the regions of the oscillations and anti-oscillations for the first and the second mode and the results of numerical simulations have proved that the second mode can be observed strictly on the condition that the sampling frequency corresponds to the oscillation intervals.

Similar to Fig. 2, we present now Fig. 9, that shows regions of oscillations for the first three spatial modes (plots (a), (b) and (c) respectively) calculated from the expressions (5). As in the previous case, there will be regions of overlapping — simultaneous oscillations of several spatial modes.

Note that if one can observe the oscillation regimes for multiple spatial modes at the same sampling frequency, the output of the PDO depends on the initial conditions and the geometric parameters of sensing and actuating systems. For the zero initial conditions and typical values of β, β', μ and μ' we consider in the paper, it is more likely that the cantilever will display a mode with a lower frequency. Thus, we expect that the third resonance can be observed clearly if the first and the second mode are in anti-oscillations.

The distribution of the oscillation amplitudes for the third mode is presented in Fig. 10 (we do not give the plots with distributions of the lower modes since they look similar to those shown in Fig. 3). There are narrow bands in the figure where the third mode amplitude is significant, and values of f_1 (or f_3) correspond precisely to the oscillation regions (see fig. 9). Note that these regions are very narrow and decay as the dissipation parameter γ increases.

The example that illustrates the dominance of the third mode at the parameters γ and f_3 taken from the gray (or oscillation) region in Fig. 10 is shown in Fig. 11. Figure 11(a) presents the limit cycles displayed by the variable $x_{i,n}$ and $v_{i,n}$. The profile of the beam is shown in Fig. 11(b). The dashed lines show the corresponded profiles of the three spatial modes and the solid line shows the actual profile of the beam.

In this part, we have demonstrated that the PDO is capable of actuating different vibration modes (or resonances) of the

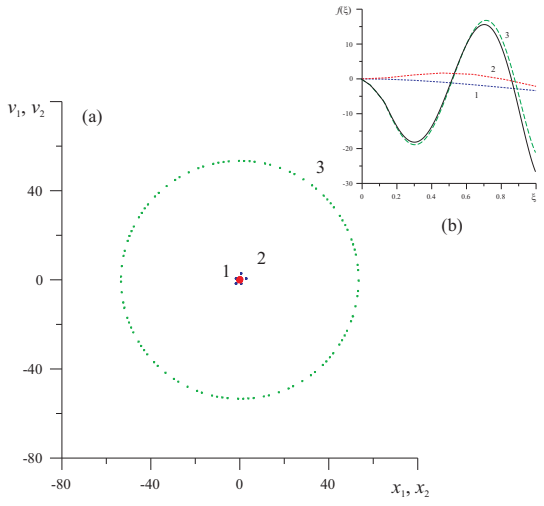

Fig. 11. (a) Typical limit cycles. (1) is the limit cycle displayed by the dynamical variables $(x_{1,n}, v_{1,n})$ that correspond to the first spatial mode, (2), (3) are the limit cycle displayed by the second and the third modes. (b) A typical profile of the beam as a function of the longitudinal coordinate ξ; The dashed lines with mark "1", "2" and "3" show the profiles that correspond to the first, second and third spatial modes; The actual profile of the beam as a superposition of the three modes is shown as the black solid line. $\gamma = 0.001$ and $f_1 = 0.75$.

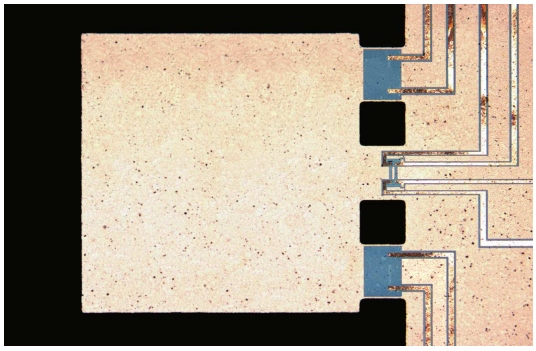

Fig. 12. Microscope photograph of the MEMS resonator. The Wheatstone bridge used to sense deflection is located in the central beam, while the resistors that actuate the device are placed in the external beams.

mechanical structure. Numerical simulations have shown that changing the sampling frequency and the sign of the feedback loop allows control of the oscillation and antioscillation regimes for a given resonance, and, as a consequence, allows actuation of higher modes. Our next step is to prove it experimentally with a PDO setup.

IV. Experimental setup

A. MEMS resonator

The MEMS resonator used in our experimental work is a silicon cantilever manufactured in a bulk micromachining process, being originally designed for gas sensing applications [19]. It consists of a squared silicon plate, with 1000 μm long, 1000 μm wide and 5 μm thick, suspended and anchored to a SOI wafer through three rectangular beams of 150 μm long and 200 μm wide (see Fig. 12). Device actuation is thermoelectrical, performed through two heating resistors placed in the outer beams. These resistors are covered by a layer of silicon oxide, so that the difference in thermal expansion coefficients between silicon and silicon oxide causes the deflection of the beam/bridge structure. Deflection sensing is done using a piezoresistive Wheatstone bridge located in the central beam. Thermal and mechanical separation between sensing and actuation structures is provided by 150 μm x 150 μm empty areas.

The frequency of the fundamental mechanical mode of this device, extracted from the process batch, is in the range between 3.88 and 5.09 kHz [19]. However, the linear theory of transversal vibrations for elastic beams can be used to obtain estimated frequency values for the three first vibration modes (see [20] or the cited formula in part I of the work [15]). Thus, for a cantilever beam with 1150 μm long, 1000 μm, 5 μm thick, and material parameters from [19], such theoretical values are 4.56 kHz for the first mode, 28.59 kHz for the second and 80.06 kHz for the third one.

Additionally, in order to obtain some additional information about the mechanical behaviour of the MEMS device, a series of FEM simulations using the Coventorware environment have been performed. These simulations are intended only to approximately obtain the frequency ranges corresponding to the vibration modes, thus second order effects concerning geometries or materials, such as uncertainty in the SOI wafer thickness or non-idealities and tolerances of the manufacturing process have not been considered. As a consequence, both the geometrical structures simulated and the results obtained are approximate but sufficient for our purposes.

Moreover, let us remark that the models and the theory of excitation of different vibration modes developed in this work apply basically to 2D MEMS devices, but the resonator used in the experiments is a true 3D device. Then, let us take into consideration here only those modes obtained from FEM simulations that exhibit a strong longitudinal component, i.e. strong enough to be captured by the sensing structure placed in the central beam of the device. According to this, Fig. 13 shows the first three vibration modes of this type, located respectively around 4.17, 28.36 and 82.65 kHz.

On the other hand, a first set of measurements have been performed in order to exactly locate the first mechanical vibration modes. To this effect velocity and displacement of different points in the resonator have been measured with a scanning Polytec MSV 400 laser-doppler vibrometer. A laser beam was pointed with the aid of a microscope down to the vibrating surface, and scattered back through the microscope objective towards the interferometric sensor. Laser Doppler signal was converted to velocity using a Polytec VD02 decoder. By monitoring several points of the device, an average measurement of displacement or velocity of the

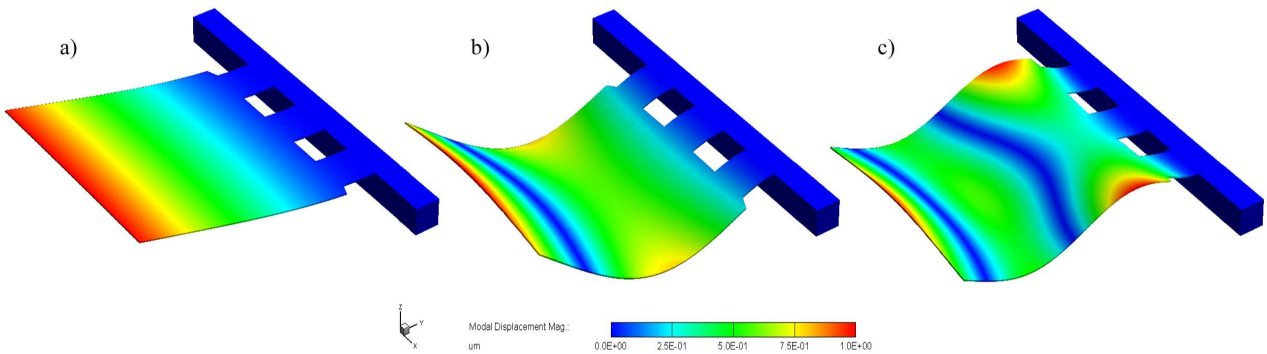

Fig. 13. First (a), second (b) and third (c) longitudinal vibration modes for the MEMS resonator structure of Fig. 12 obtained with Coventorware mechanical simulations.

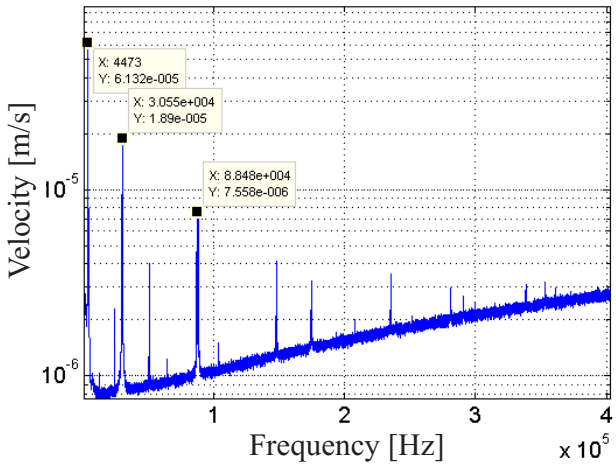

Fig. 14. Three first MEMS resonator vibration modes obtained with a vibrometer after a frequency sweep.

whole structure, in its out-of-plane motion, was obtained.

The result of this first set of measurements was the velocity spectrum of the MEMS resonator after a frequency sweep in the 0-400 kHz range. As it can be seen in Fig. 14, the resonant frequencies obtained with the vibrometer for the first three longitudinal modes (4.473 kHz, 30.55 kHz 88.48 kHz) fairly agree with the previous approaches based either on linear theory and in FEM simulations. Let us remark that all measurements made with the vibrometer equipment have been done on air conditions, thus damping losses are not negligible.

B. Experimental setup

One of the main objectives of this work is to demonstrate experimentally the feasibility of separately exciting different vibration modes in a MEMS device by setting a few parameters of a PDO structure. The experimental framework developed for this purpose, described in Fig. 15, is based on the single feedback PDO architecture with a variable number of delays. It consists of a specific analog board, which includes the MEMS actuation and sensing interface circuits plus the sign detector, and a DE2 commercial digital board

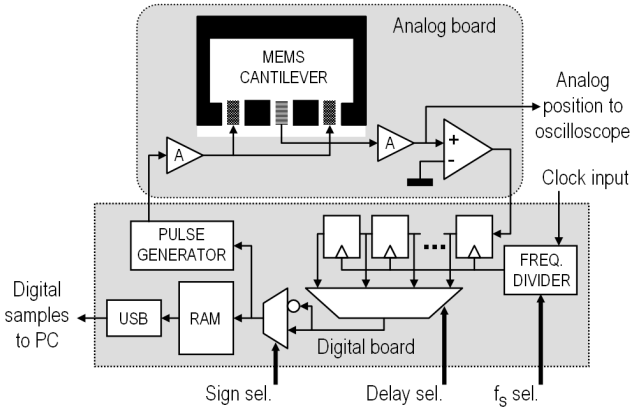

Fig. 15. Experimental setup.

from Terasic Technologies, based on a Cyclone II FPGA from Altera.

The digital system programmed in the FPGA, described in VHDL, implements the PDO digital feedback loop and the components necessary to obtain the PDO digital output, store it temporarily in an on-board SRAM and send it via USB to a computer for further processing. The switches of the board are used to easily set the PDO circuit parameters that allow to separately excite different vibration modes in the resonator, i.e. the sampling frequency (f_s) and the sign and the number of delays of the digital feedback loop L.

Let us note that one of the most important features of PDO systems is a direct digital output from their intrinsic built-in analog to digital conversion. However it is also possible to obtain data in analog format, but this requires continuous position sensing and some extra measurement equipment. Only for comparison purposes, this analog method has been also used in this work: the output signal from the instrumentation amplifier located after the MEMS position sensing structure has been sent to an oscilloscope, and a universal counter has been used to obtain the oscillation frequencies.

V. Experimental results and discussion

Since the objective of this section is to experimentally verify the theoretical expectations outlined in previous sections for the excitation of individual vibration modes with PDO structures, the first step was to configure a PDO circuit in order to excite the first vibration mode detected in Fig. 14. To this effect, a configuration was chosen that sets an oscillation regime for frequencies around 4.4 kHz, but it also puts into antioscillation regime the frequency ranges around the other two longitudinal vibration modes considered (see Fig. 9). To this effect, the sampling frequency was f_s = 139 kHz and the number of delays in the feedback loop was $L = 4$. The corresponding results, measured with a vibrometer, are shown in Fig. 16 (a). It is easy to see there that the first vibration mode is reached and that the dominant oscillation frequency is 4.46 kHz, a value very close to that obtained in Fig. 14 and to the value obtained with FEM simulations.

Then the PDO circuit was configured to separately excite the two other vibration modes detected in Fig. 14. For example, Fig. 16(b) corresponds to a configuration that sets an oscillation regime for frequencies around 30.5 kHz and sets an antioscillation regime for the frequency ranges corresponding to the other two vibration modes, thus, the sampling frequency was again f_s = 139 kHz and $L = 13$. The results shown in Fig. 16(b) suggest that the second longitudinal vibration mode was reached and it has an oscillation frequency of 30.6 kHz, a value again closer to that of Fig. 14 and to the simulations. In the same way, the third longitudinal vibration mode was successfully located at 88.41 kHz for f_s = 139 kHz and $L = 16$ (see Fig. 16(c)).

Figure 17 shows three oscilloscope screenshots of the MEMS deflection waveforms, extracted from the so-called PDO 'analog' output, for the same experimental cases as in Fig. 16. Digital channel D0 (not shown in the figure) corresponds to the sampling clock. All measurements shown in

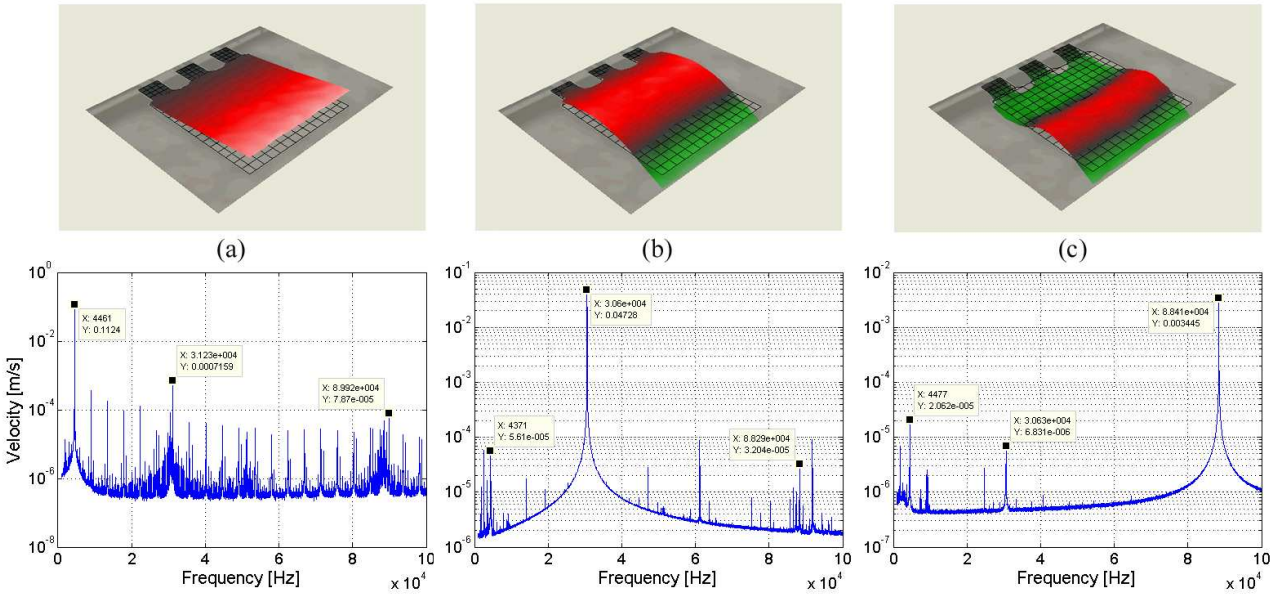

Fig. 16. Vibrometer results of cantilever deflection and velocity spectrum when the PDO system is configured to excite (a) only the first longitudinal mode of the resonator, (b) only the second one, and (c) only the third one.

Fig. 17 have been done placing the resonator inside a vacuum chamber, so they correspond to low pressure conditions around 0.1 mPa, with damping losses drastically reduced. Let us note that good sinusoidal waveforms are obtained.

On the other hand, Fig. 18 experimentally illustrates that PDO oscillation frequencies and spectra can be easily obtained from the digital output, using only standard tools for digital processing. What Fig. 18 shows is a pseudo-transient (the horizontal axis is the number of samples instead of time) of the digital frequencies obtained when changing the PDO configuration, with a fixed f_s = 139 kHz, to successively pass from the first to the second and, after, to the third vibration mode of the resonator. These digital frequencies have been obtained from the bit stream of the PDO after low pass filtering and decimation, and they allow identifying the oscillation frequency of each vibration mode. Thus, in the first step of Fig. 18.b, f_D = 0.0328, so the oscillation frequency is $f_D \cdot f_s = 4.56$ kHz, which corresponds to the first vibration mode. In the same way, we have f_D = 0.2218 and a frequency $f_D \cdot f_s$ = 30.83 kHz for the second step or vibration mode.

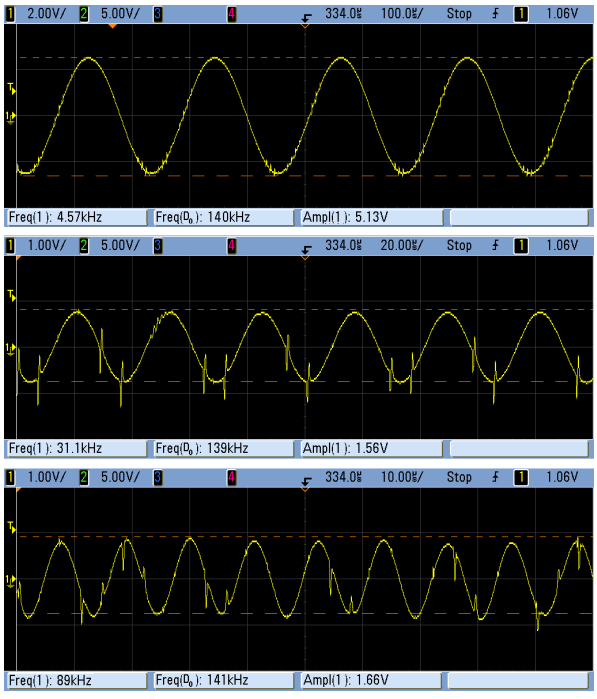

Fig. 17. Oscilloscope screen captures of the MEMS deflection waveforms corresponding to the first (up), second (middle) and third (bottom) vibration modes for the same experimental cases as in Fig. 16.

The interpretation of the third step of digital frequency shown in Fig. 18 is not straightforward. Indeed, it is already known that the third vibration mode is located at about 89 kHz and that the sampling frequency is 139 kHz, so we have a sample ratio $f_{OSC}/f_s > 0.5$ and the PDO is working in under sampling conditions. Therefore, aliasing occurs and the multiplication of spectra prevents the identification of the oscillation frequency as $f_D \cdot f_s$. However, a previous work from the authors [21] demonstrates that in PDOs working in under sampling conditions it is possible to extract the oscillation frequency when the sample ratio segment that includes f_{OSC}/f_s is already known. To this effect the following expression might be applied,

$$f_{OSC} = \begin{cases} \left(\frac{r}{2} + f_D\right) f_s, & \text{if } r \text{ is even}, \\ \left(\frac{r+1}{2} - f_D\right) f_s, & \text{if } r \text{ is odd}, \end{cases} \tag{10}$$

being r the integer part of $[2f_{OSC}/f_s]$. In our case $r = 1$ and $f_D = 0.362$, so the oscillation frequency is calculated as $(1 - f_D) \cdot f_s = 88.65$ kHz, close to the value measured for the third vibration mode of the MEMS resonator using the so-called analog method.

Finally, let us note that a good agreement exists between

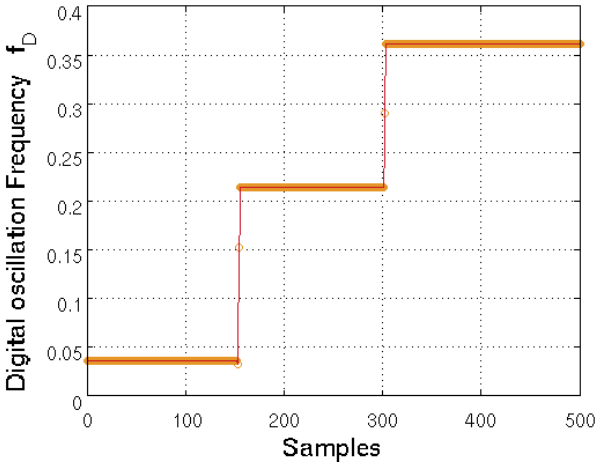

Fig. 18. Digital frequency values obtained after switching the PDO configuration to successively excite the first, second and third vibration modes of the MEMS resonator.

TABLE I

COMPARISON BETWEEN THE EXPECTED THEORETICAL, SIMULATIONS AND MEASURED FREQUENCY VALUES [KHZ] OBTAINED FOR THE FIRST THREE MODES OF THE MEMS RESONATOR

	Linear theory	FEM simulations	Vibrometer characterisation	PDO measurements
First mode	4.56	4.17	4.47	4.46
Second mode	28.59	28.36	30.55	30.60
Third mode	80.06	82.65	88.48	88.41

the theory, simulation and experimental results obtained. Such agreement is shown in table I, where theoretical, simulations and experimental results for the three vibration modes are summarized and compared.

VI. CONCLUSIONS

In this paper we have shown that spatial modes (or mechanical resonances) of the MEMS structure used in a PDO system can be controlled by a small number of parameters of such a system. We have first considered in detail the simplest, but common, case when the first two mechanical modes are taken into consideration and later incorporated the third resonance mode into the statement of the problem. We have shown the planes spanned by controlling parameters of the system with distributions of the oscillation amplitudes and frequencies and discussed at which values of the sampling frequency the excitation of higher spatial modes is possible.

This selective excitation of different vibration modes of a MEMS resonator with configurable PDO systems has also been experimentally demonstrated. Experimental results agree both with previous theory and with mechanical FEM simulations. PDO circuits with three different feedback loop configurations have been implemented and tested in order to obtain the first three longitudinal vibration modes of a MEMS resonator. In this way, it is concluded that PDO capabilities for sensing applications based on frequency shift detection are strongly improved.

VII. ACKNOWLEDGEMENTS

This work was supported by the Spanish government through the TEC2007-67951/MIC (FEDER) project and by Science Foundation Ireland.

REFERENCES

[1] N. Yazdi, F. Ayazi, and K. Najafi, "Micromachined inertial sensors," *Proceedings of the IEEE*, vol. 86, pp. 1640–1659, 1998.
[2] T. Ono and M. Esashi, "Mass sensing with resonating ultra-thin silicon beams detected by a double-beam laser Doppler vibrometer," *Measurement Science and Technology*, vol. 15, pp. 1977–1981, 2004.
[3] S. Dohn, R. Sandberg, W. Svendsen, and A. Boisen, "Enhanced functionality of cantilever based mass sensors using higher modes," *Applied Physics Letters*, vol. 86, p. 233501, 2005.
[4] M. K. Ghatkesar, V. Barwich, T. Braun, J.-P. Ramseyer, C. Gerber, M. Hegner, H. P. Lang, U. Drechsler, and M. Despont, "Higher modes of vibration increase mass sensitivity in nanomechanical cantilevers," *Nanotechnology*, vol. 18, p. 445502, 2007.
[5] X. Xia and X. Lin, "Resonance-mode effect on microcantilever mass-sensing performance in air," *Review of Scientific Instruments*, vol. 79, p. 074301, 2008.
[6] W. Zhang, R. Baskaran, and K. L. Turner, "Effect of cubic nonlinearity on auto-parametrically amplified resonant MEMS mass sensor," *Sensors and Actuators A*, vol. 102, pp. 139–150, 2002.
[7] W. Zhang and K. L. Turner, "Noise analysis in parametric resonance based mass sensing," in *Proceedongs of 2004 ASME International Mechanical Engineering Congress and Exposition*, Anaheim, California USA, 13–20 November 2004.
[8] T. Wu, W. Chang, and J. Hsu, "Effect of tip length and normal and lateral contact stifness on the flexural vibration responses of atomic force microscope cantilevers," *Microelectronic Engineering*, vol. 71, pp. 15–20, 2004.
[9] W. Chang, H. Lee, and T. Chen, "Study of the sensitivity of the first four flexural modes of an AFM cantilever with a sidewall probe," *Ultramicroscopy*, vol. 108, pp. 619–624, 2008.
[10] J. Sanchez-Rojas, J. Hernando, and et al., "Piezoelectric modal sensors/actuators based on microplates applying surface electrode patterning," in *In proc. of 15th International Conference on Solid-State Sensors, Actuators and Microsystems (TRANSDUCERS-09)*, Denver, CO, USA, June, 21-25 2009.
[11] C. Acar and A. M. Shkel, "Structural design and experimental characterization of torsional micromachined gyroscopes with non-resonant drive mode," *Journal of Micromechanics and Microengineering*, vol. 14, pp. 15–25, 2004.
[12] S. Sung, W. Sung, C. Kim, S. Yun, and Y. Lee, "On the mode-matched control of MEMS vibratory gyroscope via phase-domain analysis and design," *Transactions on Mechatronics*, vol. 14, pp. 446–455, 2009.
[13] M. Domínguez, J. Pons-Nin, J. Ricart, A. Bermejo, and E. Figueras Costa, "A novel $\Sigma - \Delta$ pulsed digital oscillator (PDO) for MEMS," *IEEE Sensors J.*, vol. 5, pp. 1379–1388, Dec. 2005.
[14] M. Domínguez, J. Pons-Nin, J. Ricart, A. Bermejo, E. Figueras Costa, and M. Morata, "Analysis of the $\Sigma - \Delta$ pulsed digital oscillator for MEMS," *IEEE Trans. Circuits Syst. I*, vol. 52, pp. 2286–2297, Nov. 2005.
[15] E. Blokhina, J. Pons, J. Ricart, O. Feely, and M. Dominguez, "Control of MEMS vibration modes with Pulsed Digital Oscillators: Part I – Theory," *IEEE Trans. Circuits Syst. I*, submitted for publication.
[16] A. Teplinsky and O. Feely, "Limit cycles in a MEMS oscillator," *IEEE Trans. Circuits Syst. II*, vol. 55, pp. 882–886, Sep. 2008.
[17] M. Domínguez, J. Pons-Nin, and J. Ricart, "General dynamics of pulsed digital oscillators," *IEEE Trans. Circuits Syst. I*, vol. 55, pp. 2038–2050, 2008.
[18] M. Domínguez, J. Pons-Nin, and J. Ricart, "Application of pulsed digital oscillators in 'reverse mode' to eliminate undesired vibrations in high-Q MEMS resonators," in *Proc. IEEE International Symposium on Circuits and Systems 2007*, New Orleans, USA, May 27–30, 2007, pp. 925–928.
[19] M. Morata, "Resonadores micromecanizados para su aplicación en la detección de gases," Ph.D. dissertation, Universitat Autònoma de Barcelona, 2004.
[20] K. Graff, *Wave Motion in Elastic Solids*. New York: Dover Publications Inc, 1975.
[21] M. Domínguez, J. Pons-Nin, J. Ricart, and E. Figueras, "The MEMS pulsed digital oscillator (PDO) below the Nyquist limit," *Sensors and Actuators A*, vol. 136, pp. 690–696, 2007.